REVISED SUBMISSION TO 'ASCE JOURNAL OF GEOTECHNICAL AND GEOENVIRONMENTAL ENGINEERING'

DATE:

03/07/2014

TITLE:

Shallow penetrometer penetration resistance

AUTHOR:

S. A. Stanier* and D. J. White**

POSITION AND AFFILIATION:

* Research Associate
** Winthrop Professor
Both based at the Centre for Offshore Foundation Systems (COFS), University of Western Australia (UWA).

CONTACT ADDRESS:

Dr. Samuel A. Stanier
Centre for Offshore Foundation Systems
University of Western Australia
M053 Fairway
Crawley
WA 6009
Australia

E-mail: sam.stanier@uwa.edu.au
Tel: +61447571092

NUMBER OF WORDS, FIGURES AND TABLES:

Words: 5543
Figures: 12
Tables: 3

KEYWORDS:

In-situ measurement; soil strength; numerical modelling; inverse analysis.

SHALLOW PENETROMETER PENETRATION RESISTANCE

S. A. Stanier and D. J. White

ABSTRACT

Shallow penetrometers - such as the hemiball and toroid - were conceived as potential in-situ testing devices with the ability to measure: (i) soil strength parameters during vertical penetration, (ii) soil consolidation characteristics during dissipation tests post-penetration and (iii) interface friction during torsional loading. Knowledge of the response of soil to such tests is critical to the design of subsea pipelines and the ability to measure the response of soil to all three types of test using a single device in-situ from a mobile testing platform, such as a Remotely Operated Vehicle (ROV), would be highly advantageous. Potential benefits of the employment of such devices could include significant time and cost savings and improved spatial measurement density, since more tests could be conducted along the route of a pipeline if an ROV is used as a mobile in-situ testing platform. This paper presents an assessment of the ability of the hemiball and toroid to measure soil strength parameters directly from their response to vertical penetration. A large deformation finite element approach was employed to model the penetration process and initial simulations were validated against small strain analyses published in the literature. A comprehensive parametric study was then conducted investigating the impact on normalized penetration resistance of soil unit weight, shear strength gradient and penetrometer-soil interface friction. A forward model was derived from the parametric analyses and its inverse performance (i.e. the ability to infer soil parameters from force-displacement response) was assessed using additional large deformation analyses with randomly assigned material parameters within realistic bounds. Both variants of shallow penetrometer investigated are found to be well suited to inferring soil strength parameters directly from their response to vertical penetration.

INTRODUCTION

As offshore oil and gas developments move into deeper waters, the requirement for pipelines and subsea facilities is increasing. This type of infrastructure – particularly pipelines – only interact with the shallowest seabed sediment (~0.5 m), the strength of which conventional penetrometers such as the cone or T-bar penetrometer are not well suited to measure. Typical cone and T-bar penetrometers are often not sensitive enough to accurately measure low near-surface strength (~1 kPa) and ought to be embedded by several diameters to achieve reliable strength measurements. The strength of this surficial sediment is a key parameter in the estimation of as-laid pipeline embedment (Westgate et al. 2012), and analysis of the sliding resistance of seabed foundations (Feng et al. 2013). Subsea pipelines also often undergo significant movement laterally and axially during operation due to the cycles of temperature and pressure as hot product passes through the pipeline (White and Cheuk, 2008). The axial resistance between the pipeline and seabed is another critical parameter in pipeline design and is controlled by the near surface soil strength. This strength changes when subjected to the pipe weight, and during pore pressure generation and dissipation during cycles of movement (Randolph et al. 2012).

Shallow penetrometers such as the hemiball and toroid (illustrated in Figure 1) have been devised to measure the soil parameters required for the design of shallowly embedded infrastructure such as pipelines and have been trialled at small scale in the geotechnical centrifuge (Yan et al. 2010). Optimum geometries for these shallow penetrometers have previously been investigated through Small Strain Finite Element (SSFE) analyses by Yan et al. (2011). This study examined the performance of fully rough shallow penetrometers in uniform soil, with SSFE analyses performed at intervals of normalized penetration depth (w/D) in the range 0.1-0.5. A hemiball of 0.4 m diameter and toroid with dimensions of D = 0.1 m and L = 0.2 m (Figure 1) are considered practical sizes for offshore in-situ SI testing from a small platform or ROV (Yan et al. 2011).

Like the conventional CPT and T-bar devices, a shallow penetrometer can be used to infer soil strength parameters from the initial penetration resistance, although these shallow devices are intended only for a limited depth range. Following penetration, pore pressure dissipation tests can be conducted to infer the consolidation characteristics of the surficial soil (Chatterjee et al. 2013). Finally – and uniquely – the shallow penetrometers can then be rotated whilst the torsional resistance is measured. This test stage can investigate both drained and undrained sliding resistance, which is highly relevant to axial pipe-soil interaction and the sliding capacity of shallow foundations.

A practical platform for deployment of these shallow penetrometers offshore would be from a seabed drilling system (e.g. Kelleher et al. 2011) or a modified work class ROV. ROV-based deployment of SI tools has been proposed as long ago as in 1983 (Geise and Kolk 1983). The recently developed geoROV unit (Machin and Edmunds, 2014) uses suction cans to temporarily and securely anchor the ROV to the seabed prior to testing. The hemiball and toroid penetrometers could be deployed from this type of system using marinised electrical drive systems to control the penetration, dissipation and torsional test phases.

This paper is concerned with the first phase of shallow penetrometer testing: inferring soil strength parameters from a measured force-displacement response. Numerical modelling is used to explore the soil property parametric space – varying the soil strength profile and unit weight – and derive a robust inverse analysis method that has practical value as a tool for converting shallow penetrometer measurements back to soil properties.

Firstly the discrete SSFE analyses of Yan et al. (2011) are compared to Large Deformation Finite Element (LDFE) analyses with continuous penetration. Following Yan et al. (2011) the soil is modelled as elasto-plastic and obeying the Tresca yield criterion with no volume change implying undrained deformation. Optimum mesh densities are determined from this benchmarking analysis, following which a full series of parametric analyses is presented concerning the frictionless and fully rough contact limits, for both the hemiball and toroid.

Soil strength profiles including uniform and linearly-varying strength with depth (i.e. normally consolidated) are considered covering a wide range of parameter combinations. Weightless and weighty cases are compared to develop a simple framework to account for soil weight and buoyancy following the method of Chatterjee et al. (2012). The LDFE analyses are then used to derive an expression describing the normalized penetration resistance (i.e. the bearing capacity factor) purely in dimensionless terms. This expression can be used in an inverse analysis to derive the mudline soil strength s_{um} and strength gradient with depth k. The ability of the inverse model is then demonstrated using randomly generated LDFE simulations within realistic soil parameter bounds. Lastly, the impact of penetrometer-soil interface roughness is considered, providing context on the suitability of the bounding frictionless and rough forward models for inferring soil strength parameters from the vertical penetration response of shallow penetrometers.

NUMERICAL TECHNIQUE

The analyses presented in this paper were performed using the Remeshing and Interpolation Technique with Small Strain (RITSS) approach (Hu & Randolph, 1998). This is an extension of the Arbitrary Lagrangian Eulerian (ALE) method (Ghosh & Kikuchi, 1991) and consists of a series of small strain analyses with periodic remeshing prior to excessive distortion of the elements within the mesh. This process preserves solution accuracy by suppressing errors at the Gauss points of the elements that are severely distorted in regions of high strain.

During the remeshing phases the Superconvergent Patch Recovery (SPR) method (Zienkiewicz & Zhu, 1992) is used to recover the stresses from the Gauss points to the nodes of the elements. The boundaries of the distorted problem are carried forward to the next step and the solution domain is then remeshed with new undistorted elements. Following this the stresses at the new Gauss point locations are interpolated from the recovered stress fields. Similarly, nodal quantities such as material properties are interpolated from the nodal

coordinates in the distorted mesh to the locations in the new undistorted mesh. This process is repeated until the desired overall displacement is achieved with displacement steps small enough to ensure that the elements do not excessively distort between the remeshing phases. The success of the RITSS methodology is highly dependent on the accuracy of the interpolation and mapping of the stress state and material properties during each remeshing phase.

In this research the RITSS method was implemented within the commercial software Abaqus via a Fortran program that controls Abaqus using a series of Python scripts. These scripts generate each small strain problem and extract the corresponding results automatically. The Fortran program then performs the necessary recovery and interpolation process to transfer stresses and material properties from the old distorted mesh to the new undistorted mesh. The application of the RITSS technique within Abaqus is described in further detail by Wang et al. (2010) and Chatterjee et al. (2012a). Remeshing performed at intervals of penetration of 1% of the penetrometer diameter was found to generate adequate results with minimal element distortion between each small strain step. Comparisons of the performance of the Abaqus based RITSS LDFE method to others such as the Coupled Eulerian Lagrangian and Arbitrary Lagrangian-Eulerian methods are provided by Hu et al. (2014) and Wang et al. (2013) respectively.

A two-dimensional axisymmetric solution domain was adopted to model vertical penetration of the shallow penetrometers. Modified six-noded second-order triangular (CAX6M) elements were used to model the soil while the penetrometers were modelled as a rigid body. Modified elements were specified since they are inherently more robust than conventional second-order elements when used in analyses involving frictional contact (Dassault Systèmes, 2011). The mesh and boundary conditions used throughout the study are shown in Figure 2. The element size along the soil surface was limited to no greater than 2% of the penetrometer diameter following Chatterjee et al. (2012b) within a zone extending two diameters from the

penetrometer. The validity of this choice was verified through a mesh convergence analysis presented later.

The analyses were performed using a total stress approach with a linear-elastic-perfectly-plastic soil model. The elastic component was given a Young's modulus, E, of 500 times the shear strength at the corresponding depth, s_{u0}, while undrained deformation with negligible volume change was ensured by setting Poisson's ratio to 0.499 (~0.5). The impact of the elastic stiffness ratio (E/s_{u0}) was checked by performing additional analyses for both the hemiball and toroid over the range of 250-5000, covering the range expected for shallow offshore clay sediments. The impact of varying the stiffness ratio over this range was negligible, indicating that the simulations were insensitive to the Young's modulus specified. This is because at the end of each Lagrangian step in the analysis process, the soil surrounding the shallow penetrometers is failing plastically for the range of stiffness ratios verified. The inbuilt Mohr-Coulomb model within Abaqus governed plastic yield, and by setting the friction angle ϕ to zero, the yield criterion was equivalent to the simple Tresca model.

Contact between the penetrometers and the soil was model using the surface-to-surface contact methodology in Abaqus, with 'hard' normal contact. The rigid penetrometer was taken as the master surface and the soil as the slave surface. For the majority of the analyses the tangential friction was modelled for the two bounding cases: frictionless ($\tau_{max} = 0$) and fully rough ($\tau_{max} = \infty$). The impact of modelling only the bounding cases of frictionless and fully rough interfaces is explored in companion analyses presented later.

Sign convention and nomenclature

The vertical load on the penetrometer, V, is normalized by area in two ways. The nominal area, which represents the full area at the widest part of the penetrometer, is given by:

$$A_{nom,\ hemiball} = \frac{\pi D^2}{4} \quad (1)$$

$$A_{nom,\ toroid} = 2\pi LD \quad (2)$$

The contact area projected onto a horizontal plane at the current depth of embedment (ignoring heave), is equal to:

$$A_{proj,\ hemiball} = \pi w\left(D - w\right) \quad (3)$$

$$A_{proj,\ toroid} = 2\pi LD' \quad (4)$$

where D' is the effective diameter for either device and is equal to:

$$D' = D\sin\theta \quad (5)$$

where θ is the semi-angle of the embedded segment of the penetrometer at the embedment depth w:

$$\theta = \cos^{-1}\left(1 - \frac{2w}{D}\right) \quad (6)$$

For weightless soil the bearing capacity factor or normalized vertical penetration resistance is expressed as the vertical load V divided by the product of the undrained shear strength at the corresponding depth s_{u0} (coincident with the depth of the invert of the penetrometer) and either the nominal or projected areas:

$$N_{c,\ nom} = V/A_{nom}s_{u0} \quad (7)$$

$$N_{c,\ proj} = V/A_{proj}s_{u0} \quad (8)$$

For all analyses the undrained shear strength of the soil model was taken as:

$$s_{u0} = s_{um} + kz \quad (9)$$

where s_{um} is the mudline strength, k is the shear strength gradient with depth and z is the depth. The dimensionless shear strength gradient is then calculated as:

$$\kappa = \frac{kD}{s_{um}} \tag{10}$$

PRELIMINARY ANALYSES

Mesh convergence analysis

A preliminary study of the effects of mesh density was conducted to: (i) compare a baseline LDFE case with the small strain analysis solutions of Yan et al. (2011) and (ii) assess the impact on the response of the minimum element size at the penetrometer-soil interface. To satisfy the first aim, the preliminary LDFE analyses used parameters matching Yan et al. (2011): the penetrometer was fully rough and the soil strength was uniform. To satisfy the second aim three separate analyses were conducted with minimum element sizes on the penetrometer-soil interface of 0.01, 0.02 and 0.04 D with the same spatial variation of element density. Figure 3 presents two interpretations of the results of the mesh convergence simulations; one normalized by the nominal area A_{nom} and the other by the projected area A_{proj}.

It is clear that larger element size on the penetrometer-soil interface (0.04 D) causes increased noise in the calculated response. This is because the solutions are highly dependent on the contact between the penetrometer and soil, particularly for the fully rough interface condition applied here. As elements come into contact with the penetrometer they are instantly bonded, thus for large element sizes these additions cause jumps in the response. Further, when the problem is periodically remeshed the contact surface area may vary slightly, hence occasional cutbacks in resistance also occur. Reducing the element size on the penetrometer-soil interface from 0.04 to 0.02 D significantly reduces the noise in the simulated response. However, it is also clear that reducing the interface element size further, from 0.02 to 0.01 D,

yields little further advantage since the responses for 0.02 and 0.01 D are practically the same. Thus the additional computational expense is not warranted and the mesh with minimum element size of 0.02 D was used in all subsequent analyses.

Excellent agreement is evident between the SSFE and LDFE analyses for both devices to depths of 0.3 to 0.4 w/D. Beyond these depths the SSFE and LDFE analyses diverge to some degree, with the SSFE analyses indicating a larger penetration resistance. The cause of this was that contact was established on a reduced surface area in the LDFE analyses compared to those for the wished-in-place cases of the SSFE analyses. The SSFE analyses thus overestimate the surface area of the penetrometer in contact with the soil because soil heave around the penetrometer is not modelled appropriately, which in turn causes an overestimation of the penetration resistance. Hereafter, all interpretation of the penetration resistance is in terms of $N_{c,\ nom}$ (Eq. 7) as this follows the practice typically adopted in expressions for pipeline bearing capacity (e.g. Chatterjee et al. 2012).

PARAMETRIC STUDY

In the following parametric study, analyses covering the ranges of parameters set out in Table 1 (hemiball) and Table 2 (toroid) were performed. Dimensionless parameters are used throughout so the results are applicable to other sizes of hemiball and toroid. For the toroid the diameter to lever arm ration L/D was taken as 2, since that is the smallest practical size for which the interference ratio is small (Yan et al. 2011). Mudline shear strengths s_{um} and shear strength gradients k were chosen such that the dimensionless strength gradient κ was spread at intervals over the range of 0 to 20 covering uniform to highly non-uniform linear profiles for both devices. Effective unit weights of 3, 5 and 7 kN/m^3 were specified for comparison to the weightless analyses, since these values cover the typical range for fine-grained deep-water sediments. The non-dimensional term $kD/s_{u,\ avg}$ proposed by Chatterjee et al. (2012) for

pipeline analyses is the dimensionless average strength gradient where $s_{u,\,avg}$ is equal to the average strength from the soil surface to a depth of 1*D*:

$$kD/s_{u,\,avg} = kD/\left(s_{um} + 0.5kD\right) \tag{11}$$

This term is bounded by 0 for k = 0 and 2 for s_{um} = 0, which makes it a useful non-dimensional parameter when fitting expressions for both the buoyancy factors (Chatterjee et al. 2012) and, as is demonstrated in this paper, the bearing capacity factor response. For each analysis the hemiball or toroid penetrometer was penetrated to a depth of 0.5 *D* from the mudline.

Effect of soil unit weight

The vertical penetration resistance of a shallow penetrometer in fine-grained soil comprises of two components: the first due to the geotechnical resistance created by the soil strength, which is expressed as a bearing capacity factor $N_{c,\,nom}$; the second is a term due to soil buoyancy as the penetrometer embeds into the seabed and displaces weighty soil. A first assumption might be that the buoyancy can be estimated via Archimedes' principle. However, numerical analyses have shown that the correction required to account for soil buoyancy for a pipeline is in fact larger than that estimated from Archimedes principle (Merifield et al. 2009; Chatterjee et al. 2012). For pipelines the proportional increase in soil buoyancy beyond Archimedes' principle is accounted using a buoyancy factor f_b, which Merifield et al. (2009) suggested is ~1.5. Chatterjee et al. (2012) used LDFE analyses to show that it varied close to ~1.5 dependent upon the dimensionless average strength $kD/s_{u,\,avg}$. The following expression was proposed:

$$f_{b,\,pipe} = 1.38 + 0.2\left(kD/s_{u,\,avg}\right) \tag{12}$$

Using the same approach, the total vertical penetration resistance of a shallow penetrometer can be expressed as:

$$\frac{V}{As_{u0}} = N_{c,\,nom} + f_b \frac{V_s}{A_{nom}} \cdot \frac{\gamma'}{s_{u0}} \tag{13}$$

where s_{u0} is the undrained shear strength at the depth of the invert of the penetrometer and V_s is the penetrometer volume submerged below the original mudline elevation, which for the hemiball and toroid respectively is:

$$V_{s,\,hemiball} = \frac{\pi w}{6}\left(3\left(0.5D'\right)^2 + w^2\right) \tag{14}$$

$$V_{s,\,toroid} = 2\pi L\left(\frac{D^2}{8}\cdot\left(2\theta - \sin 2\theta\right)\right) \tag{15}$$

112 LDFE analyses (as summarised in Table 1 and Table 2) with varying effective unit weight, soil strength profile and penetrometer roughness were used to back-calculate suitable expressions to describe f_b in terms of $kD/s_{u,\,avg}$ for both the hemiball and toroid devices. This was achieved by back-calculating f_b such that the $N_{c,\,nom}$ profiles for the weighty cases converged with the equivalent weightless solutions. Figure 4 shows the back-calculated f_b for each group of analyses for both the hemiball and toroid in comparison to the fit for the pipeline derived by Chatterjee et al. (2012) (Equation 12). New expressions were fitted to the back-calculated buoyancy factors as follows:

$$f_{b,\,hemiball} = 1.19 + 0.06\left(kD/s_{u,\,avg}\right) \tag{16}$$

$$f_{b,\,toroid} = 1.57 + 0.10\left(kD/s_{u,\,avg}\right) \tag{17}$$

The soil buoyancy on the hemiball is less enhanced relative to Archimedes compared to either the toroid or the pipeline, as the buoyancy factor f_b is smallest. The relative magnitude of the deviation from Archimedes' principle is due to the different shapes of the heave profiles. For the hemiball the axisymmetric geometry leads to radial spreading of the heave mound, resulting in a lower average height (Figure 5). In contrast the surface heave is more

pronounced for the toroid. The increase in shear strength gradient from 0 to 20 also creates a bigger change in the surface heave height for the toroid than the hemiball, which explains the difference in gradient evident between the fitting functions given in Equations 16 and 17.

For uniform soil where $\kappa = 0$ the toroid exhibits a greater buoyancy factor than an equivalent pipeline. This is because interaction of the deformation zones within the inner diameter of the toroid causes the soil to be lifted higher (Figure 5b, left side). For $\kappa = 20$, the pipeline and toroid have equal buoyancy factors, which is consistent with the narrower non-interfering internal heave zone shown on the right side of Figure 5b.

Effect of shear strength gradient

The shear strength gradient has a significant effect on the bearing capacity factor, $N_{c,nom}$, because the failure mechanism becomes shallower if the soil strength increases with depth. Additional effects arise from the downdrag of soft near-surface sediments during penetration, as well as the differences in heave shape shown in Figure 5.

Figure 6 and Figure 7 present the nominal bearing capacity factors $N_{c,\ nom}$ for both the hemiball and toroid with frictionless and fully rough interface conditions respectively for the weightless case ($\gamma' = 0$). The analyses cover a range of dimensionless gradient κ between 0 and 20, which covers the range likely to be found offshore in normally consolidated sediments. It is clear that the hemiball is affected to a greater degree than the toroid when the shear strength gradient is increased. Increasing κ from 0 to 20 causes a reduction in bearing capacity factor of 30 and 33% for the frictionless and rough hemiball analyses, versus 11 and 12% for the equivalent toroid analyses.

The causes of this apparent reduction in normalized penetration resistance are explained by a combination of two factors. Firstly, as the shear strength gradient is increased, the deformation mechanism becomes smaller and shallower, tending to favour the weaker shallower soil (Figure 5). The normalized penetration resistance, $N_{c,\ nom}$, is described in terms

of the shear strength at the depth of the invert, s_{u0}. In non-uniform soil the average strength mobilised by the deformation mechanism reduces in comparison to the strength used in the normalisation, s_{u0}, so $N_{c,nom}$ falls as the strength gradient rises. Secondly, some drag down of softer near surface sediments is evident for the profiles with linearly increasing shear strength with depth (Figure 5, right hand sides), although this is a smaller secondary effect.

Up to a depth of ~0.25 *D*, the normalized penetration resistance for the hemiball is lower than the toroid. The lever arm of the toroid causes the cross section of the deformation mechanism to be equivalent to that of a plane strain section of pipe and consequently the response simulated here is similar in shape and magnitude to that observed in the plane strain analyses of Chatterjee et al. (2012). In the pseudo plane-strain toroid analyses the soil being displaced by the penetrometer is more constrained than the perfectly axisymmetric hemiball, thus the initial rise in normalized penetration resistance is more rapid than for the hemiball.

The response of the hemiball is comparable (after accounting for the differing normalisations adopted) to those seen for a similar device in the analyses of Chatterjee et al. (2013), which used the modified cam-clay model in conjunction with the same RITSS based LDFE approach. Beyond ~0.25 *D* the hemiball has the greater normalized penetration resistance due to the response tending toward the deep solution for a deeply embedded sphere ($N_{c,\ sphere}$ = ~11.0-15.2; Randolph et al. 2000), which has a greater normalized penetration resistance than an equivalent deeply embedded plane strain pipe ($N_{c,\ pipe}$ = ~9.7-11.9; Martin and Randolph, 2006).

Calibration of a forward model

If shallow penetrometers are to be used to derive undrained soil shear strength parameters, with the assumption of a linear profile given by, s_{um} and k, it is necessary to predict the bearing capacity factor response for any dimensionless gradient κ. The following form of

equation was found to fit the normalized vertical penetration responses well for both the hemiball and toroid:

$$N_{c,\,nom} = \frac{a\left(\frac{w}{D}\right)^{b}}{c^{b} + \left(\frac{w}{D}\right)^{b}} \tag{18}$$

The numerator is of the same form as that typically used to describe the bearing capacity factor for pipelines (Aubeny et al. 2005; Chatterjee et al. 2012), while the denominator gives the form added flexibility. This enables it to capture the phenomena that are specific to the hemiball and toroid penetrometers as a result of their geometry. Parameters a, b and c are fitting parameters that have been calibrated using the LDFE results as functions of the dimensionless soil strength gradient. These fitting parameters are described in terms of the non-dimensional term, $kD/s_{u,\,avg}$ using polynomial forms:

$$a = p_1 + p_2\left(kD/s_{u,\,avg}\right) + p_3\left(kD/s_{u,\,avg}\right)^2 \tag{19}$$

$$b = p_4 + p_5\left(kD/s_{u,\,avg}\right) + p_6\left(kD/s_{u,\,avg}\right)^2 \tag{20}$$

$$c = p_7 + p_8\left(kD/s_{u,\,avg}\right) + p_9\left(kD/s_{u,\,avg}\right)^2 \tag{21}$$

The nine coefficients p_1 to p_9 have been determined for each device and for the bounding cases of frictionless and rough interfaces. This results in Equation 18 becoming a scanning equation described purely in terms of $kD/s_{u,\,avg}$. This is advantageous compared to a form described in terms of the dimensionless gradient κ, since $kD/s_{u,\,avg}$ is bounded at 0 and 2 for $k = 0$ and $s_{um} = 0$. This allows Equation 18 to be used to estimate the bearing capacity factor for any linear soil profile. Table 3 presents the calibrated coefficients p_1 to p_9, which were determined using the Levenberg-Marquardt non-linear fitting technique within Matlab.

The resultant fitted equations and the LDFE results are compared in Figure 6 and Figure 7 alongside the numerical simulations. A generally good fit is evident for all values of κ analysed. Figure 8 presents the residual error between the LDFE simulations and the estimated responses derived using Equations 18-21, described as a percentage of the mean bearing capacity factor $N_{c,\,nom}$ over the range $0 < w/D < 0.5$. The error is typically less than 5% for both penetrometers.

Inverse performance

The true test of the fitting equations presented in this paper is their application to the inverse problem; i.e. the ability to derive soil strength parameters (s_{um}, k) directly from a measured force-displacement (V, w) response, knowing only the geometry (D, L), the interface property of the penetrometer (τ_{max}) and the effective unit weight of the soil (γ'). It is assumed that the effective unit weight γ' is measured or estimated independently, and the small adjustment of the measured penetration resistance for soil buoyancy can be made prior.

To test the inverse model a further 40 simulations were performed: 10 for each penetrometer type (smooth hemiball; rough hemiball; smooth toroid and rough toroid). Combinations of soil parameters were assumed randomly within the bounds of s_{um} = 0.1-10kPa and k = 0-20 kPa/m. Effective unit γ' was assigned integer values in the range of 3-7 kN/m^3, covering the range of practical interest for pipeline design.

The force-displacement response was then processed using Matlab following the procedure described in the flowchart presented in Figure 9. Levenberg-Marquardt non-linear optimisation was used to define the parameters s_{um} and k that yielded the best fit between the inferred and simulated force-displacement response. Figure 10 summarises the performance of the inverse model over the range of parameters simulated by comparing the actual parameters - s_{um}, k, $s_{u,\,avg}$ and $kD/s_{u,\,avg}$ – to those inferred from the inverse analysis. In

general, all penetrometer variants were able to infer the mudline strength s_{um} very accurately and the gradient k with reasonable accuracy.

The reason the penetrometers are able to infer the mudline strength s_{um} more accurately than the shear strength gradient k is because at shallow embedment when w/D is very small, the shear strength gradient has only a secondary effect on the penetration resistance. The advantage of using such an inverse model is that the parameters are determined objectively.

The intention of this inverse model for shallow penetrometers is similar in essence to those developed to analyze metal indentation tests in order to extract stress-strain properties. However, such models suffer from non-uniqueness, where different combinations of elastic and plastic parameters can result in identical load-penetration responses. The inverse models for metal indentation tests are thus ineffectual at extracting stress-strain properties from load-penetration data, unless multiple indentation tests performed with indenters of differing geometry are analyzed simultaneously (Cheng and Cheng, 2004). The inverse model developed here does not suffer from the non-uniqueness problem since the simulations are insensitive to the stiffness of the soil. Different combinations of the strength parameters (s_{um}, k) may lead to the same dimensionless property ($kD/s_{u,\ avg}$) and thus the same normalized response ($N_{c,\ nom}$-w/D) but critically, always result in unique load-displacement responses (V-w).

EFFECT OF PENETROMETER-SOIL INTERFACE FRICTION

The forward models described above encompass the bounding cases of frictionless and fully rough interfaces. The effect of interface contact behaviour was investigated by performing analyses for the extreme cases of uniform ($\kappa = 0$) and highly non-uniform ($\kappa = 20$) soil. Four interface conditions were modelled: the bounding cases of frictionless and fully rough contact and two cases with frictional penalty contact. For the frictional penalty contact analyses the sliding resistance is taken as the minimum of $\mu\sigma_n$ and τ_{max}, where μ is a penalty parameter, σ_n

is the normal stress and τ_{max} is a user-defined interface shear stress limit. If the maximum allowable resistance on the interface is exceeded, then slippage between the nodes on the interface is allowed. In the first penalty contact case μ was taken as unity and τ_{max} was taken as equal to the current shear strength at the depth of the invert of the penetrometer, s_{u0}. This simulated near-rough contact but with an allowance for slippage once the interface shear stress limit was reached. In the second case μ was taken as 0.33 while τ_{max} was taken as the remoulded mudline shear strength, s_{um}/S_t. This latter scenario simulates a case where the soil in contact with the penetrometer is fully remoulded. Either of these cases is potentially plausible and provides some context for the bounding frictionless and fully rough analyses.

Figure 11 and Figure 12 present the results of the interface friction analyses for the uniform and non-uniform cases respectively. For the uniform soil (κ = 0), variation of the interface friction condition from fully rough to frictionless causes a reduction in the bearing capacity factor $N_{c,\,nom}$ of ~29% for the hemiball and ~22% for the toroid, on average. Similarly for the non-uniform (κ = 20) soil the reduction in $N_{c,\,nom}$ for the hemiball and toroid was ~25% and ~23% on average respectively. These ranges are similar to those derived for T-bar and ball penetrometers from plasticity solutions for interface friction coefficients of 0 and 1 (Martin and Randolph, 2006).

For the penalty contact analyses a different trend is apparent. For the case with $\tau_{max} = s_{u0}$ the response initially follows that of the fully rough interface condition for both penetrometers, in uniform and non-uniform soil, but becomes slightly less beyond a penetration depth of w/D = 0.25. Interrogation of the simulations at these penetration depths indicated that the shear stress on the interface had reached the limiting value so slippage occurred on the interface even though the soil in contact with the penetrometer had a higher (remoulded) strength. This caused the divergence from the fully rough analyses where slippage was prohibited.

When the interface shear stress limit was taken as $\tau_{max} = s_{um}/S_t$ an intermediate bearing capacity factor response was observed for the uniform soil that was ~20% and ~14% lower on

average than the fully rough analyses for the hemiball and toroid respectively. Similarly, for the non-uniform profiles the responses were ~21% and ~20% lower than the fully rough counterparts. However for the non-uniform profiles the $\tau_{max} = s_{um}/S_t$ analyses initially tend closer to the rough and near-rough analyses before gradually progressing towards the frictionless case with increasing penetration. This is because at low embedment the ratio of the limiting interface shear stress to the local shear strength at the depth of the invert of the penetrometer (τ_{max}/s_{u0}) is close to unity, while with increasing penetration this ratio reduces due to the effect of the shear strength gradient k increasing the local shear strength s_{u0}.

It is likely that a full-scale device for field application would be of intermediate surface roughness and thus similar in response to one of the two penalty contact analyses presented here. The two penalty contact analyses fall within the frictionless and fully rough cases for all penetrometer variants. These analyses demonstrate that the inverse application of the forward models developed in this paper provide an objective basis to assess upper and lower bound parameters for mudline shear strength, s_{um}, and shear strength gradient with depth, k, even for penetrometers of intermediate surface roughness.

CONCLUSIONS

This paper described a comprehensive suite of numerical analyses investigating the vertical penetration resistance of shallow penetrometers, focusing on the hemiball and toroid first described by Yan et al. (2010). The analyses were performed using Abaqus by following the RITSS framework, modelling the soil as an elasto-plastic material using the Tresca yield criterion. Soil strength was varied linearly with depth and a range of soil strengths and gradients were investigated so as to cover the range expected in infield conditions. The numerical technique was first benchmarked against SSFE analyses published in the literature before the effects of soil unit weight, shear strength gradient and penetrometer-soil interface friction were investigated through a parametric study. The analyses were used to derive a

forward model. The model was demonstrated to be robust when used in an inverse manner to infer soil parameters from a load-penetration response. The study has the following key outcomes:

1. Equations for correcting for the impact of soil buoyancy have been proposed in the same form as Chatterjee et al. (2012) proposed for a pipeline. These are derived in dimensionless terms using the average shear strength gradient, $kD/s_{u,\,avg}$.
2. Increasing dimensionless shear strength gradient has been found to cause an apparent reduction in normalized penetration resistance for both hemiball and toroid shallow penetrometers. This is because as the dimensionless strength gradient is increased, the deformation mechanisms favour the shallower, weaker soil, so the average mobilised strength reduces. The hemiball is affected to greater extent by this effect than the toroid due to the truly axisymmetric nature of the deformation zone compared to the pseudo plane-strain deformation zone caused by a section of a toroid.
3. A forward model has been derived in terms of the non-dimensional parameter $kD/s_{u,\,avg}$. The advantage of this approach is that $kD/s_{u,\,avg}$ is bounded at 0 and 2; so the forward model is applicable for use with any possible combination of parameters. The mathematical form of the forward model is very similar to those derived for planar pipelines, except for the additional degrees of freedom to suit the responses specific to hemispherical and toroidal shallow penetrometers.
4. The inverse performance of the forward model has been assessed using additional LDFE analyses performed with randomly selected parameters within realistic bounds. The model was demonstrated to be sufficiently robust to allow mudline strength, s_{um} and shear strength gradient, k, to be inferred from a single load-penetration response. The model is able to infer s_{um} to a greater degree of

accuracy than k, as s_{um} has a first order effect on the very shallow penetration resistance whereas k has only a second order impact. Such models are necessary if shallow penetrometers are to be used to directly measure soil parameters using vertical penetration tests in an objective manner.

5. Fully smooth and rough conditions have been demonstrated to provide lower and upper bounds to the normalized penetration resistance. Adoption of a penalty approach with and without interface shear stress limits resulted in curves that fell within the bounds. The fully smooth and rough forward models proposed here can be used to provide upper and lower bound estimates for the soil strength parameters using real shallow penetrometers in the field, which in reality would be neither fully smooth nor fully rough.

ACKNOWLEDGEMENTS

The work forms part of the activities of the Centre for Offshore Foundation Systems (COFS) at the University of Western Australia, which is supported by the Lloyd's Register Foundation as a Centre of Excellence and is a node of the Australian Research Council (ARC) Centre of Excellence in Geotechnical Science and Engineering. The second writer is supported by an ARC Future Fellowship and holds the Shell Energy and Minerals Institute (EMI) Chair in Offshore Engineering.

REFERENCES

Aubeny, C.P., Shi, H. and Murff, J.D. (2005). Collapse load for a cylinder embedded in trench in cohesive soil. International Journal of Geomechanics, 5, No. 4, 320-325.

Chatterjee, S., Randolph, M.F. and White, D.J. (2012). The effects of penetration rate and strain softening on the vertical penetration resistance of seabed pipelines. Géotechnique, 62, No. 7, 573-582.

Chatterjee, S., Randolph, M.F. and White, D.J. (2013). A parkable piezoprobe for measuring c_v at shallow depths for offshore design, Géotechnique, DOI: 10.1680/geot.13.T.008.

Cheng, Y.T. and Cheng, C.M. (2004). Scaling, dimensional analysis, and indentation measurements. Materials Science and Engineering: R: Reports, Vol. 44, No. 4-5, 91-149.

Feng, X., Randolph, M.F., Gourvenec, S. and Wallerand R. (2013). Design approach for rectangular mudmats under fully three-dimensional loading, Géotechnique, DOI: 10.1680/geot.13.P.051.

Geise, J.M. and Kolk, H.J. (1983). The use of submersible for geotechnical investigations. Proc. of Sub Tech '83. Paper 7.3, London, Society for Underwater Technology, The Design and Operation of Underwater Vehicles.

Ghosh, S. and Kikuchi, N. (1991). An arbitrary Lagrangian Eulerian finite element method of large deformation analysis of elastic-viscoplastic solids. Computational Methods in Applied Mechanical Engineering, 86, No. 2, 127-188.

Hu, Y. and Randolph, M.F. (1998). A practical numerical approach for large deformation problems in soil. International Journal of Numerical and Analytical Methods in Geomechanics, 22, No. 5, 327-350.

Hu, P., Wang, D., Cassidy, M.J. and Stanier, S.A. (2014). Predicting the resistance profile of spudcan penetrating sand overlying clay. Canadian Geotechnical Journal, Published online ahead of print, 9th May 2014. DOI:10.1139/cgj-2013-0374.

Kelleher, P., Low, H.E., Jones, C., Lunne, T., Strandvik, S. and Tjelta, T.I. (2010). Strength measurement in very soft upper seabed sediments. International Symposium on Frontiers in Offshore Geotechnics: ISFOG 2010, Perth, Australia.

Machin, J. and Edmunds, J. (2014), New generation geotechnical surveys using ROV-deployed geoROV systems. UT2 – The Magazine of the Society of Underwater Technology, No. 4, 24-25.

Martin, C.M. and Randolph, M.F. (2006). Upper bound analysis of lateral pile capacity in cohesive soil, Géotechnique **56**, No. 2, 141-145.

Merifield, R.S., White, D.J. and Randolph, M.F. (2009). Effect of surface heave on response of partially embedded pipelines on clay. Journal of Geotechnical and Geoenvironmental Engineering, ASCE 135 No. 6, 819-829.

Randolph, M.F., White, D.J. and Yan, Y. (2012). Modelling the axial resistance on deep-water pipelines. Géotechnique **62**, No. 9, 837-846.

Wang, D., Randolph, M.F. and White, D.J. (2013). A dynamic large deformation finite element method based on mesh regeneration. Computers and Geotechnics, No. 54, 192-201.

Wang, D. White, D.J. and Randolph, M.F. (2010). Large deformation finite element analysis of pipe penetration and large amplitude lateral displacement. Canadian Geotechnical Journal, 47, No. 8, 842-856.

Westgate, Z.J., White, D.J. and Randolph, M.F. (2012). Field observations of as-laid embedment in carbonate silts. Géotechnique **62**, No. 9, 787-798.

White, D.J. and Cheuk, C.Y. (2008). Modelling the soil resistance on seabed pipelines during large cycles of lateral movement. Marine Structures, 21, No. 1, 59-79.

Yan, Y., White, D.J. and Randolph, M.F. (2011). Penetration resistance and stiffness factors for hemispherical and toroidal penetrometers in uniform clay, International Journal of Geomechanics, 11, No. 4: 263-275.

Yan, Y. White, D.J. and Randolph, M.F. (2010). Investigations into novel shallow penetrometers for fine-grained soils. International Symposium on Frontiers in Offshore Geotechnics: ISFOG 2010, Perth, Australia.

Zienkiewicz, O.C and Zhu, J.Z. (1992). The Superconvergent patch recovery and posterior error estimates. Part 1: The recovery technique. International Journal of Numerical Methods in Engineering, 33, No. 7, 1331-1364.

NOMENCLATURE

a	model parameter
A	area
A_{nom}	nominal area
A_p	projected area
b	model parameter
c	model parameter
d	model parameter
D	diameter
D'	effective diameter
D_0	outer diameter
f_b	buoyancy factor
γ'	effective unit weight
k	shear strength gradient
κ	dimensionless shear strength gradient
L	lever arm
$N_{c,nom}$	nominal bearing capacity factor
$N_{c,\,pipe}$	bearing capacity factor for a deeply embedded pipe
$N_{c,proj}$	projected bearing capacity factor
$N_{c,\,sphere}$	bearing capacity factor for a deeply embedded sphere
p_n	constant
ϕ	friction angle
S_t	sensitivity
s_{u0}	undrained shear strength
$s_{u,avg}$	average undrained shear strength
s_{um}	undrained shear strength at the mudline

μ penalty contact parameter

θ angle

τ_{max} limiting shear stress

T torque

V vertical force

V_s submerged volume

w vertical embedment

LIST OF TABLES

LIST OF FIGURES

Figure 10: Performance of inverse model at predicting parameters: (a) mudline shear strength s_{um}, (b) shear strength gradient with depth k, (c) average shear strength over a depth of $1D$ $s_{u,avg}$, and the non-dimensional parameter $kD/s_{u,avg}$.

Figure 11: Effect of interface roughness in uniform soil ($\kappa = 0$): (a) hemiball and (b) toroid penetrometer.

Figure 12: Effect of interface roughness in non-uniform soil ($\kappa = 20$): (a) hemiball and (b) toroid penetrometer.

TABLES

Table 1: Summary of hemiball analyses conducted in the parametric study.

D (m)	s_{um} (kPa)	k (kPa/m)	kD/s_{um}	$s_{u,avg}$ (kPa)	$kD/s_{u,avg}$	γ' (kN/m^3)	$\gamma' D/s_{um}$
0.4	10	0	0	10	0	0,3,5,7	0.12, 0.20, 0.28
0.4	8	2	0.1	8.4	0.1	0,3,5,7	0.15, 0.25, 0.35
0.4	2	2	0.4	2.4	0.33	0,3,5,7	0.60, 1.00, 1.40
0.4	2	2.5	0.5	2.5	0.4	0,3,5,7	0.60, 1.00, 1.40
0.4	1	5	2	2	1	0,3,5,7	1.20, 2.00, 2.80
0.4	0.8	10	5	2.8	1.43	0,3,5,7	1.50, 2.50, 3.50
0.4	0.2	10	20	2.2	1.82	0,3,5,7	6.00, 10.00, 14.00

Table 2: Summary of toroid analyses conducted in the parametric study.

D (m)	L (m)	s_{um} (kPa)	k (kPa/m)	kD/s_{um}	$s_{u,avg}$ (kPa)	$kD/s_{u,avg}$	γ' (kN/m^3)	$\gamma' D/s_{um}$
0.1	0.2	10	0	0	10	0	0,3,5,7	0.03, 0.05, 0078
0.1	0.2	2	2	0.1	2.1	0.1	0,3,5,7	0.15, 0.25, 0.35
0.1	0.2	1	4	0.4	1.2	0.33	0,3,5,7	0.30, 0.50, 0.70
0.1	0.2	1	5	0.5	1.25	0.4	0,3,5,7	0.30, 0.50, 0.70
0.1	0.2	0.5	10	2	1	1	0,3,5,7	0.60, 1.00, 1.40
0.1	0.2	0.2	10	5	0.7	1.43	0,3,5,7	1.50, 2.50, 3.50
0.1	0.2	0.1	20	20	1.1	1.82	0,3,5,7	5.00, 5.00, 7.00

Table 3: Coefficients for normalised vertical resistance expressions for frictionless and rough hemiball and toroid penetrometers for $w/D \leq 0.5$.

Contact	Penetrometer	Coefficients								
		p_1	p_2	p_3	p_4	p_5	p_6	p_7	p_8	p_9
Frictionless	Hemiball	7.18	0.87	-0.71	1.24	-0.45	0.16	0.24	0.10	-0.01
	Toroid	6.77	-1.53	0.49	0.67	0.09	-0.08	0.17	-0.13	0.05
Rough	Hemiball	10.10	-0.71	0.07	1.35	-0.56	0.15	0.25	-0.03	0.07
	Toroid	7.81	-2.20	0.80	0.88	0.18	-0.21	0.13	-0.09	0.02

FIGURES

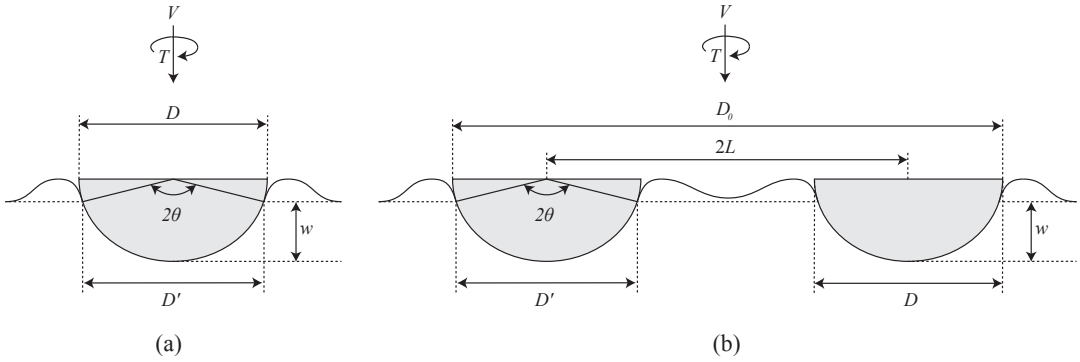

Figure 1: Schematic and nomenclature of devices: (a) hemiball and (b) toroid penetrometers.

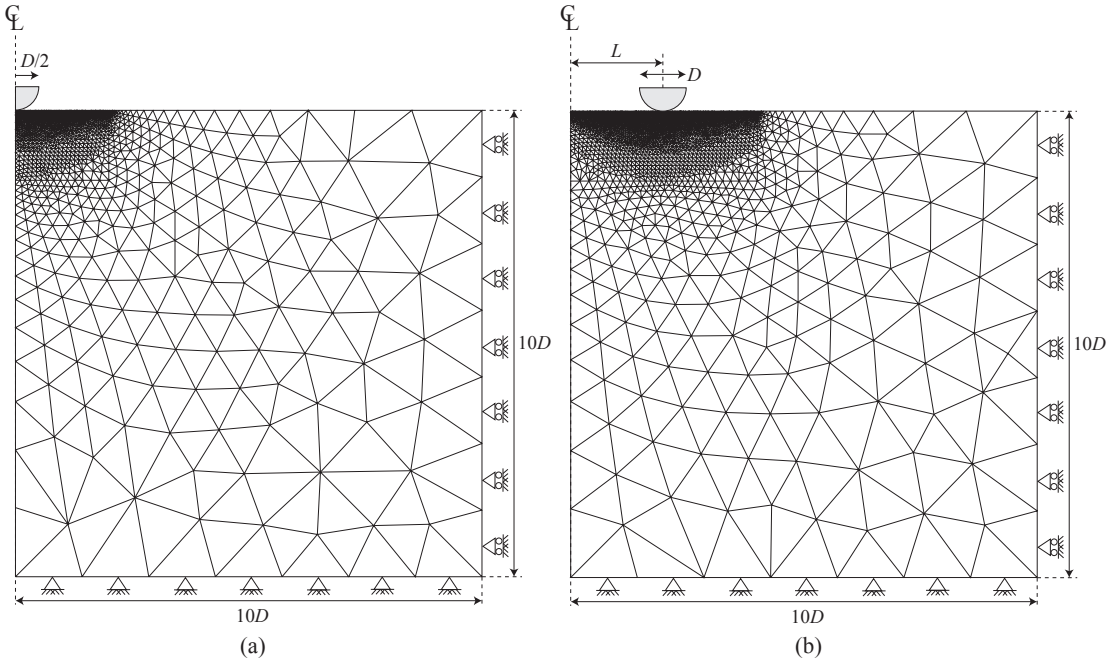

Figure 2: Analysis mesh and boundary conditions: (a) hemiball and (b) toroid penetrometers.

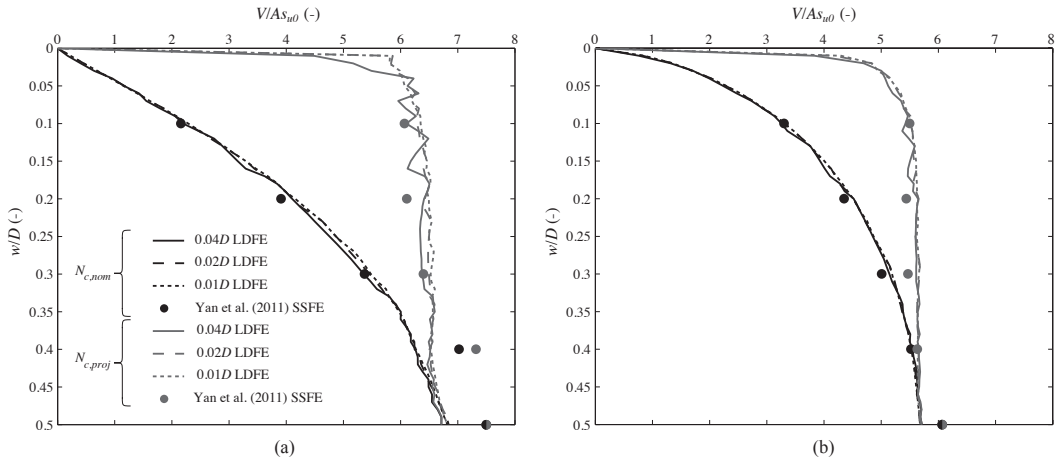

Figure 3: Mesh convergence check and comparison with previous small-strain analyses; uniform soil with a fully rough interface: (a) hemiball and (b) toroid.

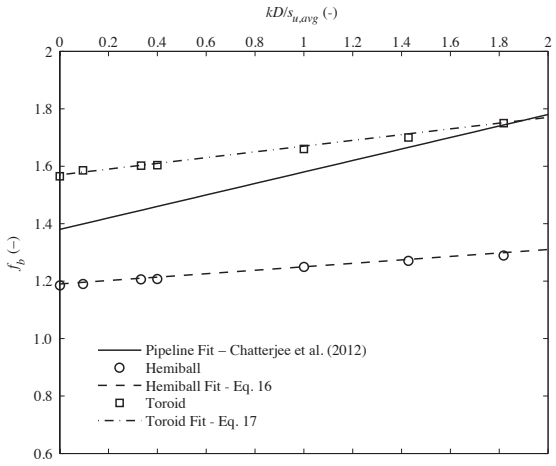

Figure 4: Variation of buoyancy factor f_b for hemiball and toroid penetrometers and pipelines.

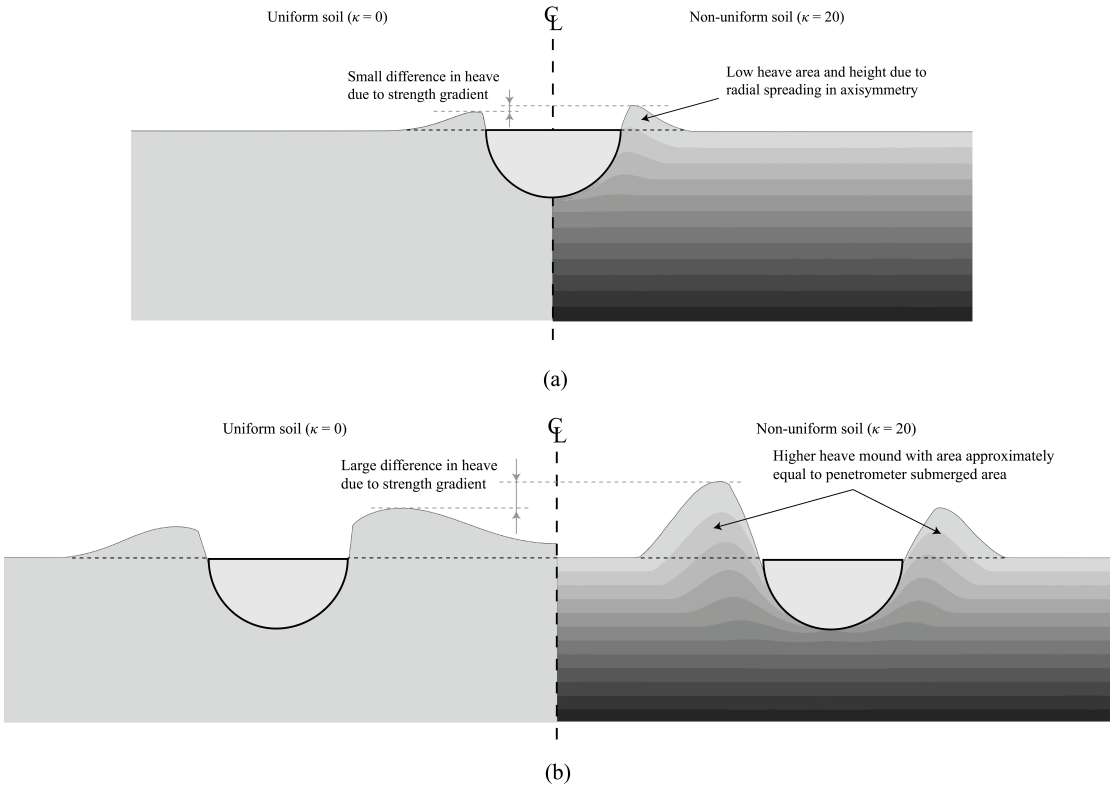

Figure 5: Effect of shear strength gradient on surface heave profiles at w/D of 0.5 in uniform (κ = 0) and non-uniform (κ = 20) soil for (a) hemiball and (b) toroid penetrometers.

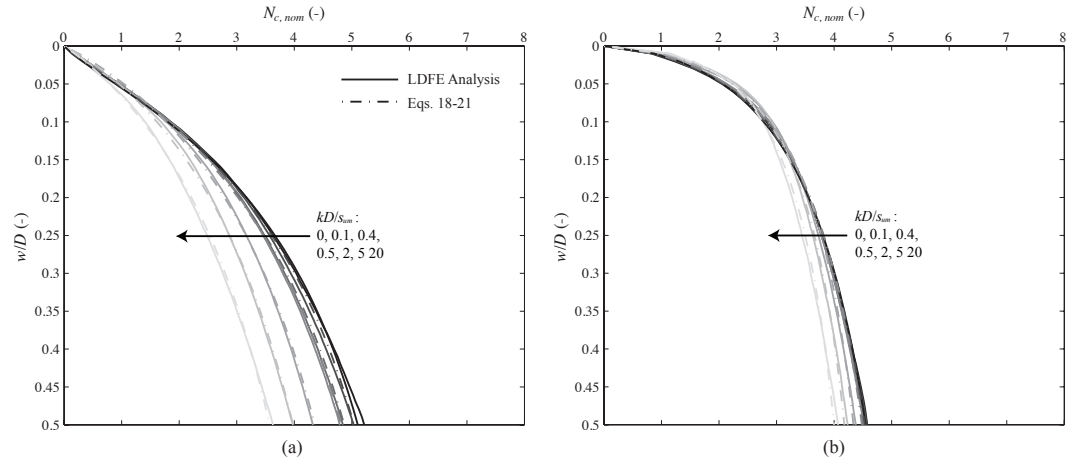

Figure 6: Effect of shear strength gradient for a frictionless penetrometer interface: (a) hemiball and (b) toroid penetrometer.

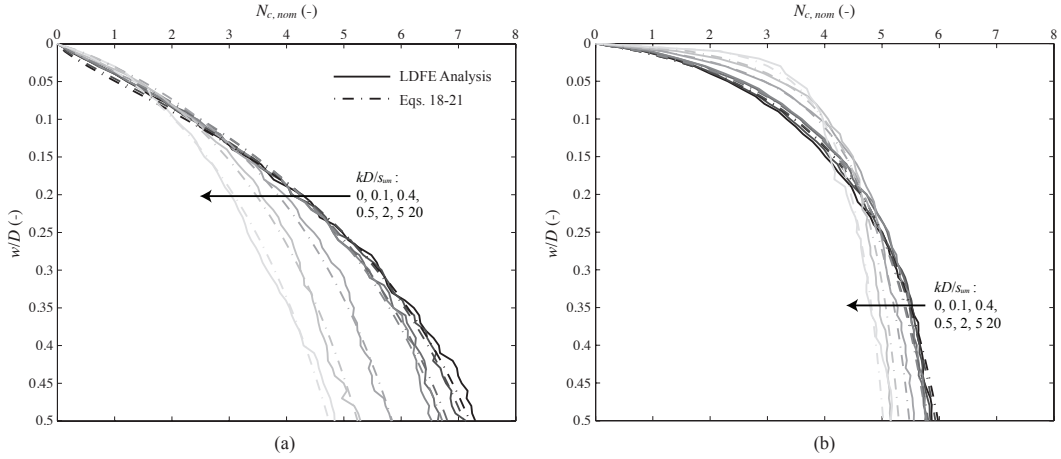

Figure 7: Effect of shear strength gradient for rough penetrometer interface: (a) hemiball and (b) toroid penetrometer.

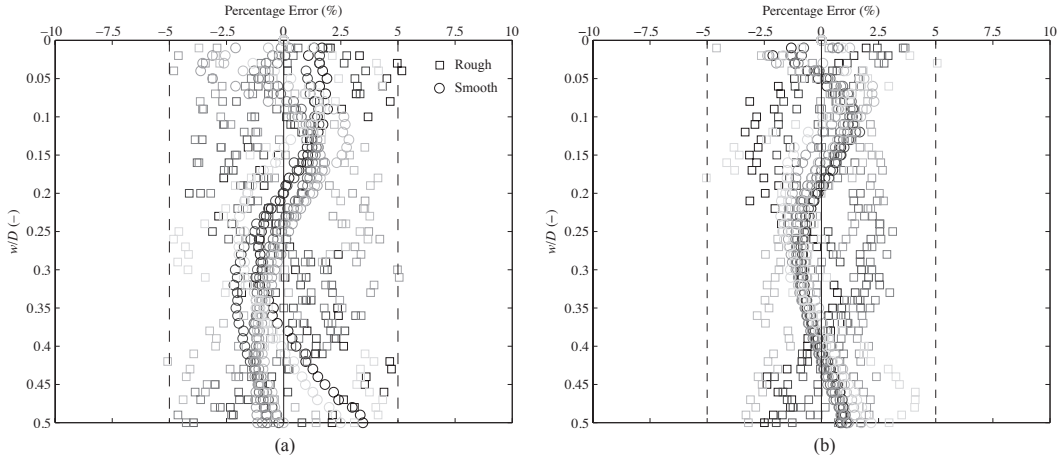

Figure 8: Residual error from fitting equations presented as a percentage of the mean $N_{c,\,nom}$: (a) hemiball and (b) toroid residual error.

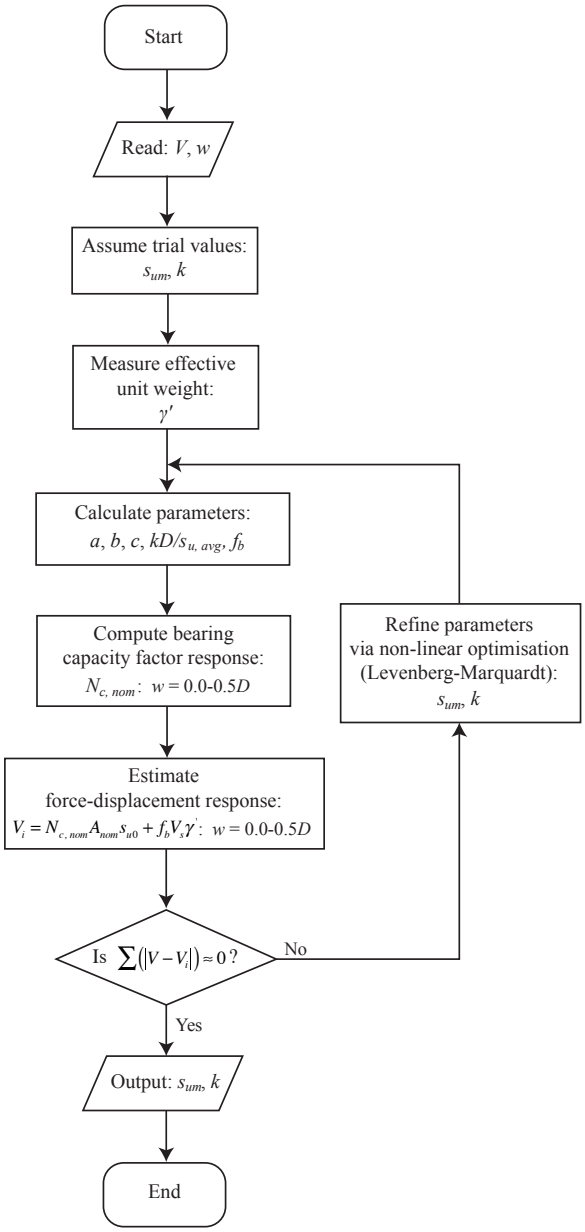

Figure 9: Flow chart for inverse model to objectively infer soil strength parameters.

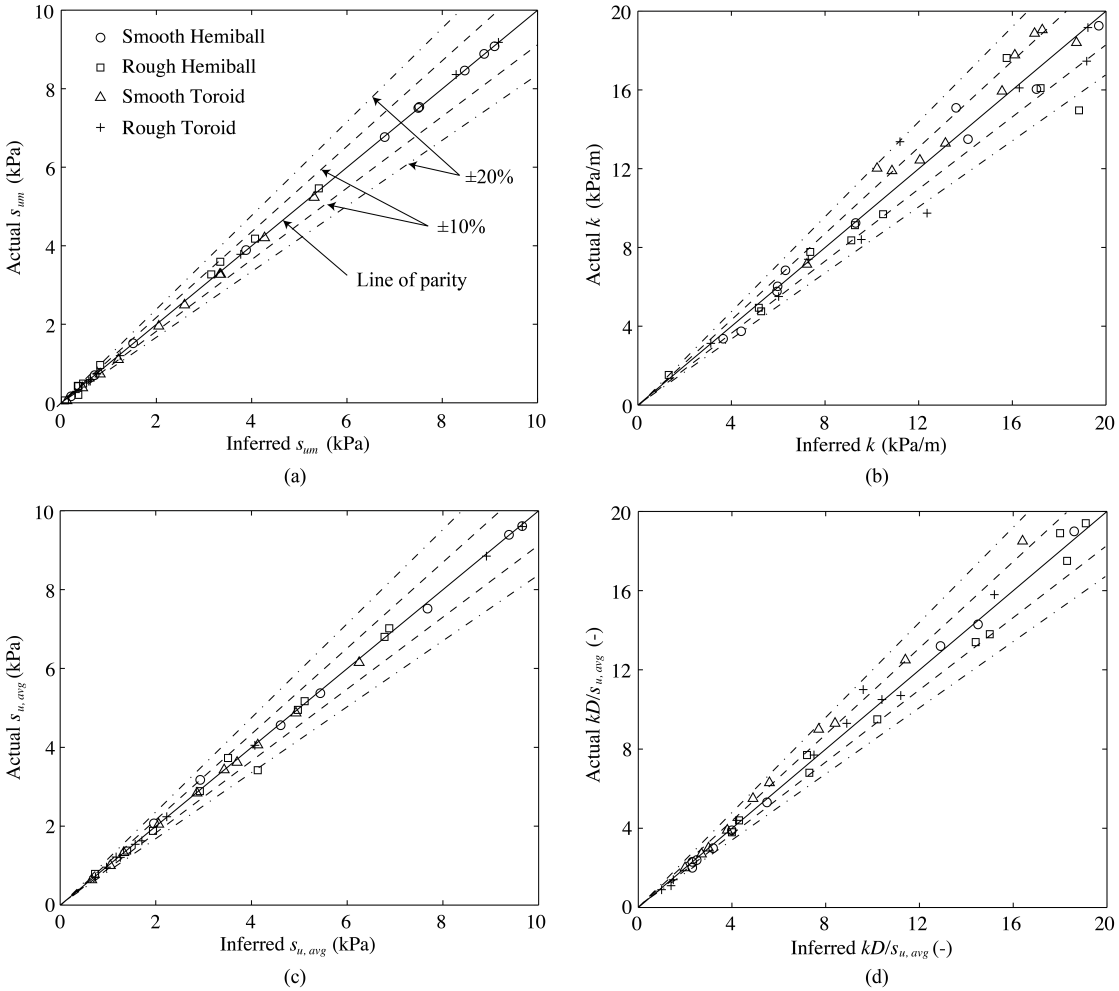

Figure 10: Performance of inverse model at predicting parameters: (a) mudline shear strength s_{um}, (b) shear strength gradient with depth k, (c) average shear strength over a depth of 1D $s_{u,avg}$, and the non-dimensional parameter $kD/s_{u,avg}$.

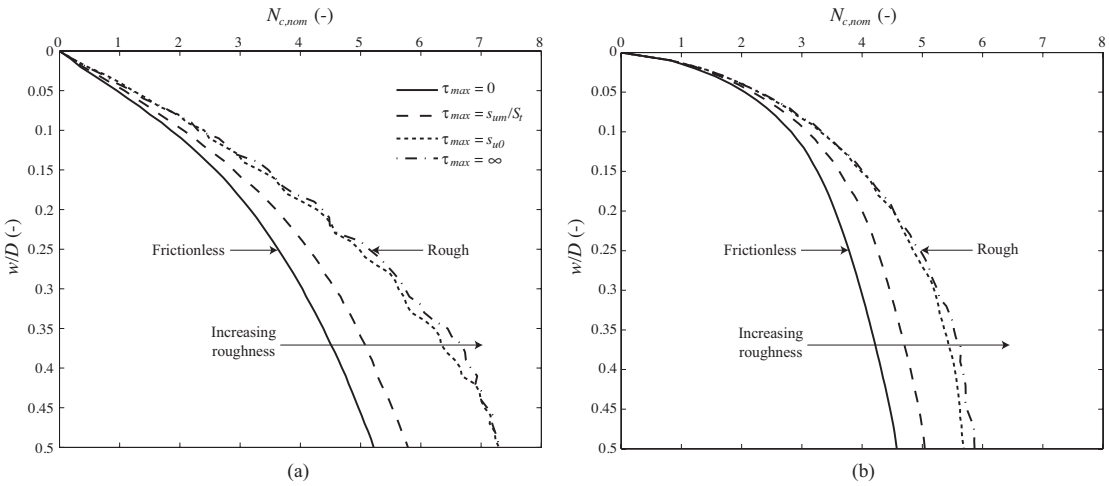

Figure 11: Effect of interface roughness in uniform soil (κ = 0): (a) hemiball and (b) toroid penetrometer.

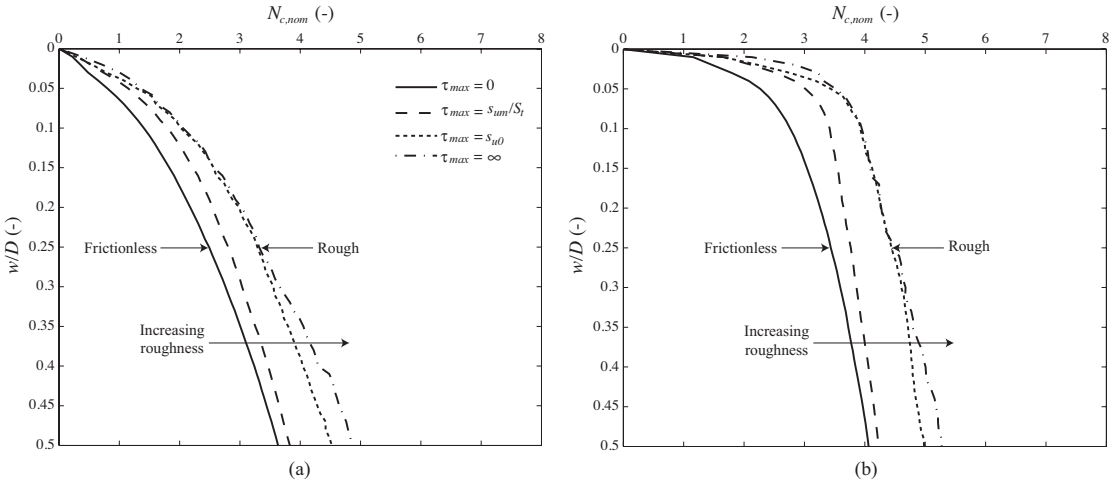

Figure 12: Effect of interface roughness in non-uniform soil (κ = 20): (a) hemiball and (b) toroid penetrometer.